Vector field microscopic imaging of light

K. G. LEE[1], H. W. KIHM[1], J. E. KIHM[1], W. J. CHOI[2], H. KIM[3], C. ROPERS[4], D. J. PARK[1], Y. C. YOON[1], S. B. CHOI[1], D. H. WOO[5], J. KIM[6], B. LEE[3], Q. H. PARK[2], C. LIENAU[4,7] AND D. S. KIM[1]*

[1]Department of Physics and Astronomy, Seoul National University, Seoul 151-747, Korea
[2]Department of Physics, Korea University, Seoul 136-701, Korea
[3]School of Electrical Engineering, Seoul National University, Seoul 151-747, Korea
[4]Max-Born-Institut für Nichtlineare Optik und Kurzzeitspektroskopie, D-12489 Berlin, Germany
[5]Korea Institute of Science and Technology, Seoul 136-791, Korea
[6]Korea Research Institute of Standards and Science, Taejon 305-600, Korea
[7]Carl von Ossietzky Universität Oldenburg, Institut für Physik, D-26111 Oldenburg, Germany
*e-mail: dsk@phya.snu.ac.kr

The behaviour of nanoscale optical devices in a variety of burgeoning research areas, such as photonic crystals[1–4], near-field microscopy[5–7], surface plasmonics[8–11] and negative index of refraction materials[12–16], is governed by strongly localized electromagnetic waves. Although such light waves are analogous to the localized electronic wavefunctions that determine the properties of solid-state quantum devices, unlike matter waves, these optical fields are vectorial in nature, and their orientation and magnitude vary on a subwavelength scale. In order to obtain a complete description of light in nanoscale devices, it is therefore crucial to be able to map the field vectors with subwavelength resolution. Thus far, local field vectors have mostly been studied by theoretical means. Here, we describe and demonstrate the first experimental mapping of vector fields of light on the nanoscale. By directly accessing the local field in its entirety, new capabilities and applications in nanophotonics may emerge.

Maxwell's electromagnetic theory of light was in large part inspired by Faraday's curved, moving lines of force traversing all space[17,18]. Although the harmonic electromagnetic plane wave, first derived by Maxwell, is characterized by a single polarization vector, both the magnitude and orientation of the electric field generally depend on position: $E(r, t)=\text{Re}[E(r)e^{i\omega t}]$. Here $E(r)$ is the local electric field at every position and ω is the angular frequency.

Strong local variations of the electric-field vector are an essential characteristic of light in any nanostructure, as was shown, for example, in the pioneering work using polarization-varying near-field microscopy[6]. More recently, a polarization-sensitive sheet of organic molecules was proposed as a sensitive probe in determining the longitudinal electric-field component of Bessel beams[19]. In the following, we present three examples representing, to our knowledge, the first mapping of nanoscale vector fields. This vector mapping uses a scattering-type near-field microscopic technique[20,21], combined with complete tip characterization.

We first map the electric-field vector of evanescent standing waves generated by total internal reflection of two counter-propagating incident beams inside a prism (Fig. 1a). We use a chemically etched glass-fibre tip functionalized with a 100-nm-diameter gold nanoparticle[22] (Fig. 1b). The light

scattered by this tip into the far-field region is polarization-analysed. The polar plots of the scattered light, shown in Fig. 1b, for horizontal and vertical incident polarizations suggest that this functionalized tip serves as an excellent probe for measuring local polarization, with the principal axes being aligned close to the x and z axes. The polarization induced on the gold nanoparticle by a local electric field can then be written as[23]

$$p(r) = \begin{pmatrix} \alpha_x & 0 \\ 0 & \alpha_z \end{pmatrix} E(r) \qquad (1)$$

Here, α_x and α_z are the polarizabilities along the x and z axes, respectively. In the data shown in Fig. 1b, α_z/α_x is 1.18 at a wavelength of 780 nm, implying that the attached gold nanoparticle is slightly elliptical in shape[24]. When the tip is near the dielectric interface, it is generally expected that the intricate interaction of the probe with matter in the near-field zone can create further polarization components. It is also expected, however, that scattering from the gold nanoparticle is still dominated by the induced polarization given by equation (1), apart from some higher-order correctional terms depending on the particle size[25]. Thus the induced dipole radiation from the gold nanoparticle carries the full information about the local vector state of the electric field. Figure 1c shows a raster scan image of the scattered photon intensity, obtained by rotating the analysing polarizer by 360° at every position. Polar plots at several selected positions are displayed below the image. The long axis of the polar plot, with corrections accounting for the ellipticity of the nanoparticle, directly indicates the orientation and magnitude of the field at this position. This enables us to perform a vector-field mapping in the x–z plane (bottom, Fig. 1c). Hereafter, we represent the polar plot at every point by a single double-arrowed vector oriented along the long axis. This single vector describes the local field well as long as the local field is linearly polarized or strongly elliptically polarized.

Figure 1d and e displays the theoretical and experimental vector-field maps within a 600 nm × 300 nm scan area. The field vector rotates as we move along the x direction and the electric lines of force are explicitly visualized. For an evanescent standing

53
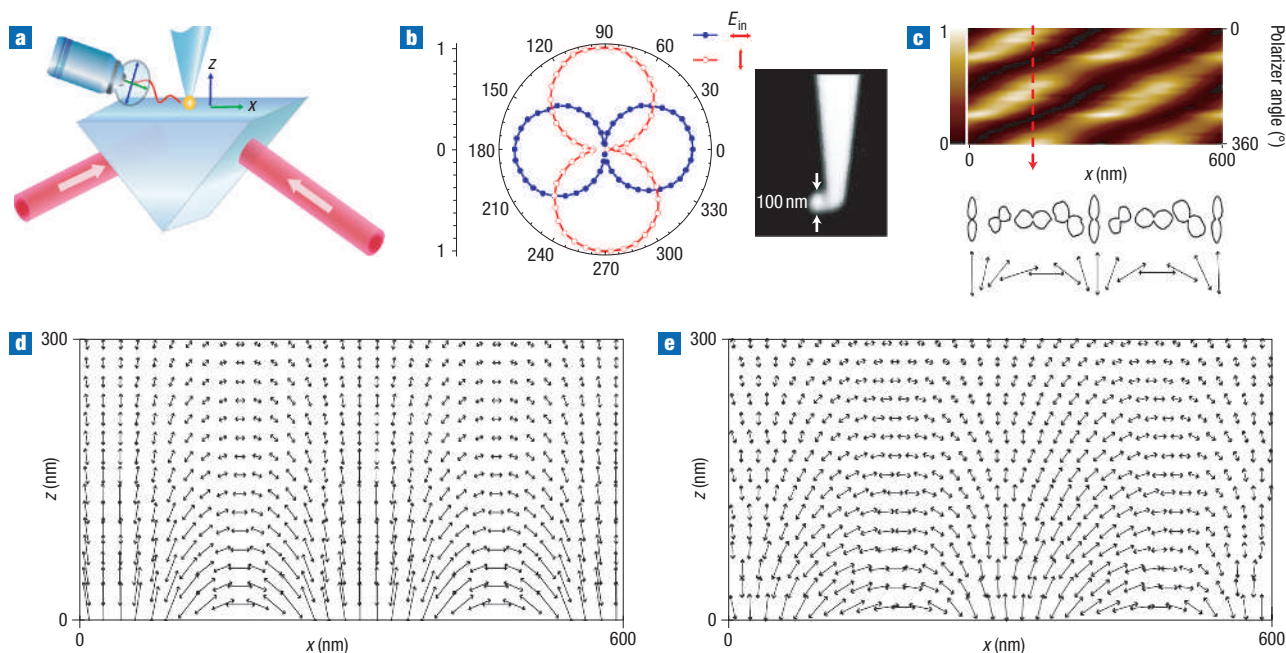
Figure 1 Vector-field mapping of an evanescent standing wave. a, Experimental setup. A surface standing wave is created by total internal reflection of two equal-intensity *p*-polarized laser beams of 780-nm wavelength inside a prism. The incidence angles are ±60°. The light scattered off a gold nanoparticle at the apex of a fibre tip is polarization-analysed. **b**, Polar plot showing tip scattering at horizontal (blue circles) and vertical (red circles) incident light polarizations, respectively. Right panel: a scanning electron microscopy (SEM) image of the tip used in our experiments. **c**, A near-field raster-scan image of the scattered light intensity. At every position, the polarization analyser is rotated by 360°. Polar plots of the scattered light at a few selected positions are shown below, together with double-arrow vector plots of the long axes, normalized to the far-field scattering data shown in **b**. **d,e**, Vector-field plots of an *x*−*z* area (600 nm × 300 nm) of the theoretical and experimental results respectively.

wave, generated by two counter-propagating *p*-polarized beams of equal intensity, the field vector is given by

$$\boldsymbol{E}(\boldsymbol{r}) = (E_x, 0, E_z) = E_0 \left(\cos kx, 0, -\frac{k}{\kappa} \sin kx \right) e^{-\kappa z} \qquad (2)$$

where E_0 is a constant magnitude, k and κ are related by the Helmholtz equation, $k^2 - \kappa^2 = (\omega/c)^2$, and are determined by the angle of incidence and the index of refraction of the prism. Experiment and theory are in convincing agreement, demonstrating the vector-field mapping technique on dielectric–air interfaces.

We now proceed to mapping surface-plasmon polariton standing waves at the interface between a flat gold surface and air (Fig. 2a). These standing waves are generated by launching counter-propagating surface-plasmon polariton waves from two adjacent nanohole gratings, separated by the flat gold film. The generation and propagation processes are described in detail in ref. 26. The electric field of this standing wave can be written in the same form as equation (2), but now with a much larger k/κ ratio equal to $\sqrt{(-\varepsilon_m)}$ where ε_m is the dielectric constant of gold:

$$\boldsymbol{E}(\boldsymbol{r}) = (E_x, 0, E_z) = E_0 (\cos kx, 0, -\sqrt{-\varepsilon_m} \sin kx) e^{-\kappa z} \qquad (3)$$

With a value of ε_m of about −25 at a wavelength of 780 nm, the surface-plasmon polariton field points mainly along the *z* axis, with a much weaker electric field along the *x* axis. In addition, the image charge of the nanoparticle induced on the metal surface

can negatively affect the *x* component scattering even further. To obtain a good vector-field image in this situation, it is necessary to have a tip that is more sensitive to the *x* component of the field. When used in scattering geometry, an apertured commercial tip was found to fulfil this requirement, having approximately twice the sensitivity to the *x*-axis field intensity, as shown in Fig. 2b, possibly because apertured tips have relatively flat apexes.

Figure 2c shows a raster-scan image of the flat metal surface with the analysing polarizer being rotated by 360°. The intensity maximum occurs near a detector polarization angle of 90°, which corresponds to the electric-field vector pointing along the *z* axis. Shown in Fig. 2d is the vector-plot image of a scan area of 1,140 nm × 500 nm in the *x*−*z* plane, with the total electric-field intensity $|E_x|^2 + |E_z|^2$. Figure 2e presents a theoretical vector plot of an area of 250 nm × 100 nm. Equation (3) appears to be in quite good agreement with the experimental results corresponding to the same area, as presented in Fig. 2f. In both cases, the electric field points predominantly along the *z* axis and switches into the *x* direction only around the total intensity $|E_x|^2 + |E_z|^2$ minima.

We now focus on the excitation of surface-plasmon polaritons when light transmits through a single slit (Fig. 3a). This generation process is particularly sensitive to the vectorial nature of light[27], because the polarization characteristics of the transmitted beam and the generated travelling surface-plasmon polariton waves are expected to be markedly different. Displayed in Fig. 3b is a near-field raster-scan image. The electric field on top of the slit is clearly oriented along the *x* axis, because the intensity maxima occur near analyser angles of 0°, 180° and 360°.
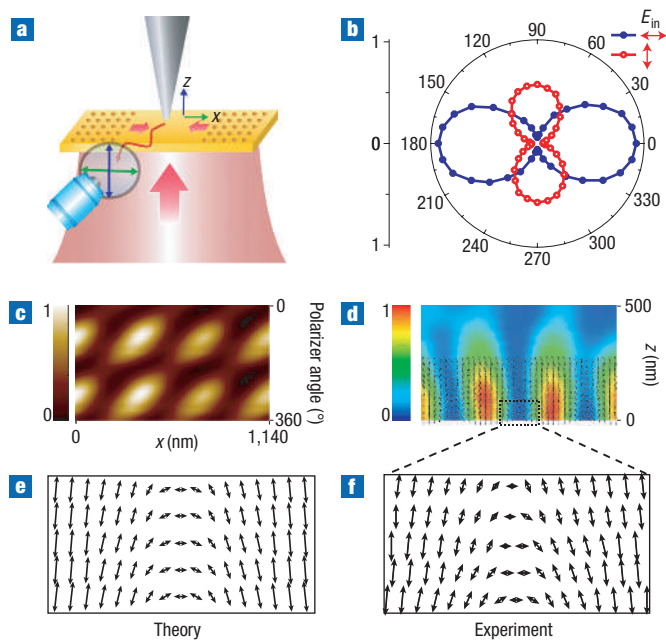
Figure 2 Vector-field mapping of the surface-plasmon polariton standing wave. a, Experimental geometry. Counter-propagating surface-plasmon polariton waves are created at two adjacent nanohole gratings perforated into 300-nm thick gold film and separated by 10.6-μm-long flat gold film. The arrays are illuminated from the bottom by a 780-nm Ti:Sapphire laser, polarized along the x-axis and focused to a spot size of about 50 μm. A metal-coated commercial tip with a nominal aperture size of 100 nm is used to map the vector field. **b**, Polar plot of the light scattered off the metal tip for the horizontal (blue circles) and vertical (red circles) incident polarization. **c**, Raster-scan image of the scattered light, rotating the analyser polarization. **d**, 1140 nm × 500 nm area scan image of the total electric-field intensity (blue-to-red colour scale) and electric-field vector. **e**, Theoretical vector plot of a 250 nm × 100 nm area, centred around a total electric-field intensity minimum. **f**, Experimental vector-plot of the same area as in **e**, and highlighted as a box in **d**.

As we move away from the centre of the slit, the intensity maxima occur at different analyser angles, suggesting that the vector rotates towards the z direction. Also, the electric-field intensity is strongly asymmetric in the near field.

Shown in Fig. 3c is a full vector-field image of the electric field emanating from this single slit. The total electric-field intensity is plotted on a blue-to-red colour scale. Along the slit axis, the decay of the E_x component with increasing z is gradual. On the flat metal surface, however, the E_z component decays much more rapidly. This rapid decay and the finding that the field is mainly oriented along the z axis suggest that we are indeed observing the generation and propagation of surface-plasmon polariton waves as light is emerging from the slit[27]. These results are in qualitative agreement with the finite-difference time-domain (FDTD) technique[28] calculations for an asymmetric single slit (Fig. 3d), revealing both the slower decay of the E_x component along the slit axis and the rotation of the electric-field vector outside the slit. The main discrepancy between experiment and theory is that the experimentally measured field is not completely oriented along the z axis, even on the flat metal surface away from the slit. This discrepancy most likely originates from the interference between the light scattered from the gold nanoparticle and a small amount of residual background light stemming from the reflection from the glass-fibre tip.
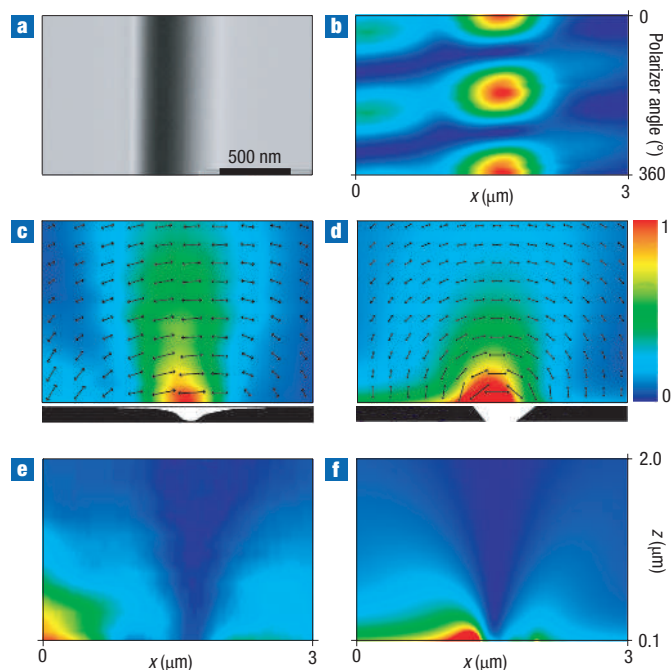
Figure 3 Vector-field mapping of light emerging from a single slit. a, An SEM image of the single slit, showing the asymmetric slit shape. **b**, Constant-height scan image at $z = 100$ nm, rotating the polarizer by 360°. **c**, Vector-field image of a 3 μm × 2 μm area starting from $z = 100$ nm, together with the total electric field intensity plot on a blue−red colour scale. At the bottom is shown an atomic force microscopic image of the slit profile. **d**, An FDTD calculation assuming an asymmetric trapezoidal slit shape. **e**, Experimental $|E_z|^2$ plotted on a (different) blue−red colour scale. **f**, Theoretical $|E_z|^2$ profile.

Plotting $|E_z|^2$ separately in Fig. 3e (experiment) and 3f (theory) makes it clear that, indeed, the E_z component decays much faster than the E_x component. The fact that surface-plasmon generation is stronger on the left side, which has a sharper edge, indicates that the higher generation efficiency originates from charge localization at sharp edges. This interesting observation of asymmetric surface-plasmon generation clearly warrants further experimental and theoretical studies.

Our results provide unprecedented images of light on the nanoscale and demonstrate that the vector-field mapping of light is indeed possible for nanosystems where spatially varying field orientations on a subwavelength scale are the rule rather than the exception and crucial for the functionality of nanophotonic devices. The first results reported in this letter describe imaging of two different vector components of the light field. Conceptually, an extension to a full three-dimensional imaging of the vector state seems straightforward, requiring the use of two independent, orthogonally oriented polarization detectors. Such tools carry the potential for making vector-field mapping for nanoscale devices a common laboratory practice that can find wide applications in physics, engineering, chemistry, and biology.

METHODS

SAMPLE FABRICATION

gold film grown on a $\lambda/5$ flat sapphire substrate. The optical axis of the substrate is perpendicular to the metal surface to avoid birefringence effects. The hole diameter and grating period are 125 nm and 761 nm, respectively. The single slit is patterned by a focused ion beam machine (QUANTA 200-3D, FEI, USA) on a piece of a 200-nm-thick gold film. The slit width is 200 nm at the bottom and 600 nm at the top. The cross-sectional profile is steeper on the left- than on the right-hand side (Fig. 3a).

EXPERIMENTAL SETUP AND DATA ACQUISITION

The scattered signal from the tip was collected by a long working distance objective lens (Mitutoyo M Plan Apo 10×, Edmund Optics, Singapore) and then passed through a spatial filter with a detection area of only a few μm^2. This detection area was monitored using a CCD camera to control tip and sample positions. The signal was measured by a silicon avalanche photodiode detector (C4777-01, Hamamatsu Photonics, Japan) combined with a lock-in (model 5210, EG&G, USA) amplifier. A linear polarizer was placed in front of the signal detector and rotated by 360° at every position in step sizes of 10°. To create evanescent optical standing waves, two counter-propagating 780-nm p-polarized laser beams of equal intensity were directed at normal incidence onto the two facets of the prism. For exciting surface-plasmon polariton standing waves at the surface of a flat gold film, the excitation beam was normally incident on the back of the sample and polarized along the x axis. For the single slit experiment, the incident polarization was perpendicular to the slit axis. An apertured commercial tip (Cr/Al coating, with nominal aperture size 100 nm) was purchased from Nanonics Imaging. A gold nanoparticle was attached to an HF-etched glass tip (FS-SN-4224, Thorlabs, USA) after chemical (3-aminopropyl-triethoxysilanes, Sigma Aldrich, USA) treatment. A home-built shear force mode near-field scanning optical microscope in tip scanning mode was used for scanning and tip attachment.

References

1. Yablonovich, E. Inhibited spontaneous emission in solid-state physics and electronics. *Phys. Rev. Lett.* **58,** 2059–2062 (1987).
2. John, S. Strong localization of photons in certain disordered dielectric superlattices. *Phys. Rev. Lett.* **58,** 2486–2489 (1987).
3. Noda, S., Chutinan, A. & Imada, M. Trapping and emission of photons by a single defect in a photonic bandgap structure. *Nature* **407,** 608–610 (2000).
4. Joannopoulos, J. D., Meade, R. D. & Winn, J. N. *Photonic Crystals* (Princeton, New York, 1995).
5. Pohl, D. W., Denk, W. & Lanz, M. Optical stethoscopy: Image recording with resolution $\lambda/20$. *Appl. Phys. Lett.* **44,** 651–653 (1984).
6. Betzig, E. & Chichester, R. J. Single molecules observed by near-field scanning optical microscope. *Science* **262,** 1422–1425 (1993).
7. Betzig, E., Trautman, J. K., Weiner, J. S., Harris, T. D. & Wolfe, R. Polarization contrast in near-field scanning optical microscopy. *Appl. Opt.* **22,** 4563–4568 (1992).
8. Ebbesen, T. W., Lezec, H. J., Ghaemi, H. F., Thio, T. & Wolff, P. A. Extraordinary optical transmission through sub-wavelength hole arrays. *Nature* **391,** 667–669 (1998).
9. García-Vidal, F. J. & Martín-Moreno, L. Transmission and focusing of light in one-dimensional periodically nanostructured metals. *Phys. Rev. B* **66,** 155412 (2002).
10. Hibbins, A. P., Evans, B. R. & Sambles, J. R. Experimental verification of designer surface plasmons. *Science* **308,** 670–672 (2005).
11. Maier, S. A. et al. Local detection of electromagnetic energy transport below the diffraction limit in metal nanoparticle plasmon waveguides. *Nature Mater.* **2,** 229–232 (2003).
12. Veselago, V. G. The electrodynamics of substances with simultaneously negative values of ε and μ. *Sov. Phys. Usp.* **10,** 509–514 (1968).
13. Pendry, J. B. Negative refraction makes a perfect lens. *Phys. Rev. Lett.* **85,** 3966–3969 (2000).
14. Shelby, R. A., Smith, D. R. & Schultz, S. Experimental verification of a negative index of refraction. *Science* **292,** 77–79 (2001).
15. Grigorenko, A. N. et al. Nanofabricated media with negative permeability at visible frequencies. *Nature* **438,** 335–338 (2005).
16. Fang, N., Lee, H., Sun, C. & Zhang, X. Sub-diffraction-limited optical imaging with a silver superlens. *Science* **308,** 534–537 (2005).
17. Maxwell, J. C. in *The Dynamical Theory of the Electromagnetic Field* (ed. Torrance T. F.) 4–10 (Wipf and Stock Publishers, Eugene, Oregon, 1996).
18. Faraday M. *Experimental Researches in Electricity* Vol. 1, 380–386 (Dover Publications, New York, 1965).
19. Grosjean, T. & Courjon, D. Photopolymers as vectorial sensors of the electric field. *Opt. Express* **14,** 2203–2210 (2006).
20. Zenhausern, F., O'Boyle, M. P. & Wickramasinghe, H. K. Apertureless near-field optical microscope. *Appl. Phys. Lett.* **65,** 1623–1625 (1994).
21. Kawata, S. & Inouye, Y. Scanning probe optical microscopy using a metallic probe tip. *Ultramicroscopy* **57,** 313–317 (1995).
22. Kalbrenner, T., Ramstein, M., Mlynek, J. & Sandoghdar, V. A single gold particle as a probe for apertureless scanning near-field optical microscopy. *J. Microsc.* **202,** 72–76 (2001).
23. Bouhelier, A., Beversluis, M. R. & Novotny, L. Near-field scattering of longitudinal fields. *Appl. Phys. Lett.* **82,** 4596–4598 (2003).
24. Kalbrenner, T., Håkanson, U. & Sandoghdar, V. Tomographic plasmon spectroscopy of a single gold nanoparticle. *Nano Lett.* **4,** 2309–2314 (2004).
25. Lévêque, G., Colas des Francs, G. & Girard, C. Polarization state of the optical near field. *Phys. Rev. E* **65,** 036701 (2002).
26. Kim, D. S. et al. Microscopic origin of surface-plasmon radiation in plasmonic band-gap nanostructures. *Phys. Rev. Lett.* **91,** 143901 (2003)
27. Lalanne, P., Hugonin, J. P. & Rodier, J. C. Theory of surface plasmon generation at nanoslit apertures. *Phys. Rev. Lett.* **95,** 263902 (2005).
28. Yee, K. S. Numerical solution of initial boundary value problems involving Maxwell's equations in isotropic media. *IEEE Trans Ant. Prop.* **14,** 302–307 (1966).

Competing financial interests

The authors declare that they have no competing financial interests.